



Article

# Boron-Implanted Silicon Substrates for Physical Adsorption of DNA Origami

Sadao Takabayashi <sup>1</sup>, Shohei Kotani <sup>1</sup>, Juan Flores-Estrada <sup>1</sup>, Elijah Spears <sup>1</sup>, Jennifer E. Padilla <sup>1</sup>, Lizandra C. Godwin <sup>1</sup> , Elton Graugnard <sup>1</sup>, Wan Kuang <sup>2</sup>, Scott Sills <sup>3</sup> and William L. Hughes <sup>1,\*</sup>

<sup>1</sup> Micron School of Materials Science & Engineering, Boise State University, Boise, ID 83725, USA; sadaotakabayashi@u.boisestate.edu (S.T.); shoheikotani@u.boisestate.edu (S.K.); juanfloresestrada@u.boisestate.edu (J.F.-E.); elijahspears@u.boisestate.edu (E.S.); jenniferepadilla@boisestate.edu (J.E.P.); lizandragodwin@boisestate.edu (L.C.G.); eltongraugnard@boisestate.edu (E.G.)

<sup>2</sup> Department of Electrical & Computer Engineering, Boise State University, Boise, ID 83725, USA; wankuang@boisestate.edu

<sup>3</sup> Micron Technology, Inc., 8000 South Federal Way, Boise, ID 83707-0006, USA; ssills@micron.com

\* Correspondence: willhughes@boisestate.edu; Tel.: +1-208-426-4859

Received: 23 July 2018; Accepted: 23 August 2018; Published: 24 August 2018



**Abstract:** DNA nanostructures routinely self-assemble with sub-10 nm feature sizes. This capability has created industry interest in using DNA as a lithographic mask, yet with few exceptions, solution-based deposition of DNA nanostructures has remained primarily academic to date. En route to controlled adsorption of DNA patterns onto manufactured substrates, deposition and placement of DNA origami has been demonstrated on chemically functionalized silicon substrates. While compelling, chemical functionalization adds fabrication complexity that limits mask efficiency and hence industry adoption. As an alternative, we developed an ion implantation process that tailors the surface potential of silicon substrates to facilitate adsorption of DNA nanostructures without the need for chemical functionalization. Industry standard 300 mm silicon wafers were processed, and we showed controlled adsorption of DNA origami onto boron-implanted silicon patterns; selective to a surrounding silicon oxide matrix. The hydrophilic substrate achieves very high surface selectivity by exploiting pH-dependent protonation of silanol-groups on silicon dioxide (SiO<sub>2</sub>), across a range of solution pH values and magnesium chloride (MgCl<sub>2</sub>) buffer concentrations.

**Keywords:** molecular self-assembly; DNA nanotechnology; DNA origami; electrostatics; semiconductor

## 1. Introduction

The semiconductor industry has followed Moore's observation that the number of components per integrated circuit would increase exponentially with time [1,2]. This trend has been reinforced by decades of top-down scaling of photolithography. Today, 193 nm immersion lithography prints up to  $\sim 10^{14}$  features in a single exposure, at spatial pitches down to 80 nm [3]. Below the diffraction limit of light, 40 and 20 nm pitches are routine with self-aligned double patterning (SADP) [4] and quadruple patterning (SAQP) [5]. While extreme ultraviolet lithography is projected to extend direct-print lithography to a 32 nm pitch [6], SADP is still required to extend it below 20 nm [7]. In response to the escalating cost of photolithography [8–10], directed self-assembly (DSA) of block copolymers (BCP) have been explored [11–16]. While compelling, critical challenges have gated adoption of DSA-BCP technology as a volume manufacturing technology. First, its line edge roughness and critical dimension uniformity are too high when compared to traditional lithography. In addition, macro-molecular defects are very difficult to characterize in real-time during manufacturing. To overcome these

challenges, programmable molecules such as DNA are starting to be explored as an alternative to BCP for patterning sub-lithographic features [17–20]. With a theoretical feature resolution of ~3 nm [21,22], and the ability to incorporate programmable optical defect metrology [23], DSA of DNA origami [24] or bricks [25] offers potential for sub-10 nm patterning [26–28].

Similar to block copolymers, DNA selectively adsorbs onto surfaces with favorable thermodynamic interactions. Adsorption is directed by pre-patterning a substrate with regions, or boundaries, that chemically differentiate favorable and unfavorable binding sites. For example, Sarveswaran et al. adsorbed DNA origami onto a positively charged self-assembled monolayer (SAM) that was pre-patterned on a silicon substrate [29]. Binding and non-binding sites were differentiated using aminopropyltrimethoxysilane (APTES) and a native oxide, respectively. In contrast, Gopinath et al. attached DNA origami onto a pre-patterned silicon dioxide substrate with negatively charged functional groups [30]. The binding and non-binding sites were differentiated using silanol and hexamethyldisilazane (HMDS) [30].

In general, surface differentiation via SAM layers is not desirable because it increases the complexity of the system and becomes a source of additional defects [31]. An alternative to SAM functionalization is to differentiate the surface using pre-patterned materials [32,33]. While DNA routinely adsorbs onto negatively charged mica surfaces [24,34], the binding strength of the DNA is non-uniform on the surface because of heterogeneous ionic exchange [35]. As an alternative to mica, Kershner et al. physically adsorbed DNA origami onto electron-beam patterned and topographically isolated diamond-like carbon sites [32]. Although their approach produced elevated surface densities, diamond-like carbon is sensitive to its processing conditions and not always amenable to DNA adsorption [30]. Instead of growing a layer of material onto a substrate surface, altering the silicon surface property is a simpler approach to promote DNA origami adsorption.

To bring directed self-assembly of DNA closer to semiconductor manufacturing, we developed a boron-implantation process to tailor the surface potential of silicon substrates for physical adsorption of DNA origami. Physical adsorption of the origami was studied as a function of the deposition buffer pH, as well as the  $MgCl_2$  concentration. Origami adsorption was characterized as a function of pH on: (I) A boron-implanted silicon substrate, and (II) a thermally grown silicon dioxide ( $SiO_2$ ) substrate. Industry standard 300 mm wafers were also patterned in a semiconductor manufacturing facility with boron-implanted silicon features separated by a  $SiO_2$  matrix. Selective adsorption of DNA origami was then demonstrated on the implanted silicon surface with no deposition on  $SiO_2$ .

## 2. Results

DNA origami triangles were modified from a previously reported study [24], as described in Supplement S1, and custom boron-implanted and  $SiO_2$  p-type silicon wafers were prepared by Micron Technology, as described in Supplement S2. The boron-implanted silicon substrate was characterized using X-ray Photoelectron Spectroscopy (XPS), Secondary Ion Mass Spectroscopy (SIMS), Transmission Electron Microscopy (TEM), and spectroscopic ellipsometry. According to XPS analysis of the as-received wafer, a 2–3 nm boron-rich oxide layer had formed within the substrate surface during the annealing process. As seen in Figure 1a, SIMS analysis of the as-received wafer showed that the boron concentration was ~14.6 atomic percent (at. %) at the surface, well beyond the <1 at. % solubility limit ( $\sim 1 \times 10^{20}$  per  $cm^3$ ) [36–38], and that the majority of the implanted boron was within ~7 nm of the surface. Figure 1b shows a cross-sectional TEM image of the as-received boron-implanted silicon substrate prepared by focused-ion beam (FIB) sectioning. The image reveals two layers above the bulk crystalline silicon, and the combined thickness of these layers agrees with the boron-rich region of the SIMS depth profile, which is colored to match the layers observed in the TEM image. Fast-Fourier Transforms (FFTs) of the layers in the TEM image revealed that the boron-rich surface layers were both amorphous. The outer layer appears inhomogeneous in the TEM cross-section images, possibly revealing boron precipitates within the boron-rich amorphous oxide [38,39]. Given the very high concentration of implanted boron, a boron-silicon phase is expected

to have formed at the interface of the amorphous layer and the crystalline silicon [40], and this layer is known to be resistant to etching in hydrofluoric acid (HF), although the etch rates depend strongly on the etchant and boron concentration [40,41]. After cleaning the substrate with Piranha and 1:100 hydrofluoric acid (Piranha + HF, Supplement S1), the boron concentration at the substrate surface was determined to be  $\sim 2.5$  at. %, which still exceeds the solubility limit of boron in silicon and represents the boron-rich amorphous layer. The resulting boron-rich layer was uniformly distributed over a  $\sim 1$  cm  $\times$  1 cm area of the substrate surface, based on XPS. For characterization details, see Supplement S3. The boron-implantation greatly reduced the hydrophobicity of the substrate surface, as shown in Supplement S4. Similarly, a boron and phosphorus co-doped silicon surface is also hydrophilic and is known to possess negative potential [42]. Thus, we expect that the boron-implanted silicon substrate also possesses a surface potential.

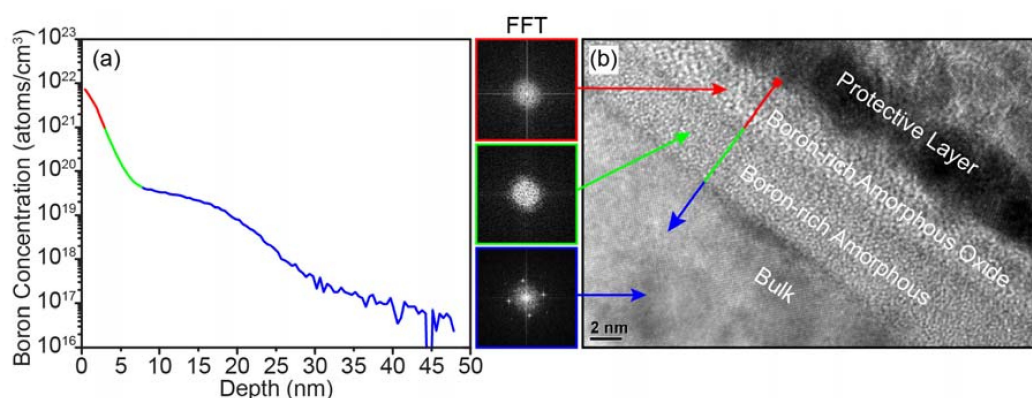


**Figure 1.** The Secondary Ion Mass Spectroscopy (SIMS) and cross-sectional Transmission Electron Microscopy (TEM) analyses of the boron-implanted silicon substrate revealed: (a) The boron concentration depth profile, and (b) structure of the substrate. The boron concentration at the surface of the substrate was  $\sim 14.6$  atomic percent, and the majority of the boron was found within  $\sim 7$  nm from the surface. The red, green, and blue colors on the plot (a) and the line in (b) correspond to the boron-rich amorphous oxide layer, the boron-rich amorphous layer, and the bulk silicon, respectively. The cross-sectional TEM image and the Fast-Fourier Transforms (FFTs) of the image showed that both outer layers were amorphous, and that the bulk was crystalline. The platinum protective layer was deposited onto the substrate surface prior to fabrication of the TEM specimen using focused-ion beam (FIB).

DNA origami triangles were deposited onto freshly cleaned boron-implanted silicon substrates with a deposition buffer using the procedure described in Supplement S1. As seen in Figure 2a, uniform, high density deposition of DNA origami triangles was observed. The average surface density ( $q_{ave}$ ) of DNA origami triangles was  $90 \pm 6/\mu\text{m}^2$ . While the average surface density was statistically comparable to that of naturally occurring mica, the adsorption uniformity was greater (see Supplement S5). The DNA origami were incubated with the substrate for  $\sim 24$  h since this incubation time was observed to give the highest surface density, as shown in Supplement S6. For longer deposition times, the density decreased by  $\sim 20\%$ , likely due to changes in the surface chemical state. Since the time needed to reach monolayer DNA origami deposition depends on the origami concentration, shorter deposition times are expected for higher DNA origami concentrations during incubation. For the DNA nanostructure counting protocol, see Supplement S7.

The concentration of divalent magnesium ions is known to strongly affect the properties of DNA nanostructures, especially deposition onto substrates. DNA origami triangles were deposited onto boron-implanted silicon substrates to study how the  $\text{MgCl}_2$  concentration ( $[\text{MgCl}_2]$ ) in the deposition buffer impacted the average surface density. The  $[\text{MgCl}_2]$  was varied from 0–35 mM and the deposition buffer pH was held constant at 6.6. As shown in Figure 2, DNA origami did not adhere at 0 mM and

the average surface density increased from 0 to  $90 \pm 6$  per  $\mu\text{m}^2$  as the  $[\text{MgCl}_2]$  increased from 0 to 35 mM. Similar to deposition on mica, the deposition on the boron-implanted Si wafers shows a strong dependence on the  $[\text{MgCl}_2]$ .

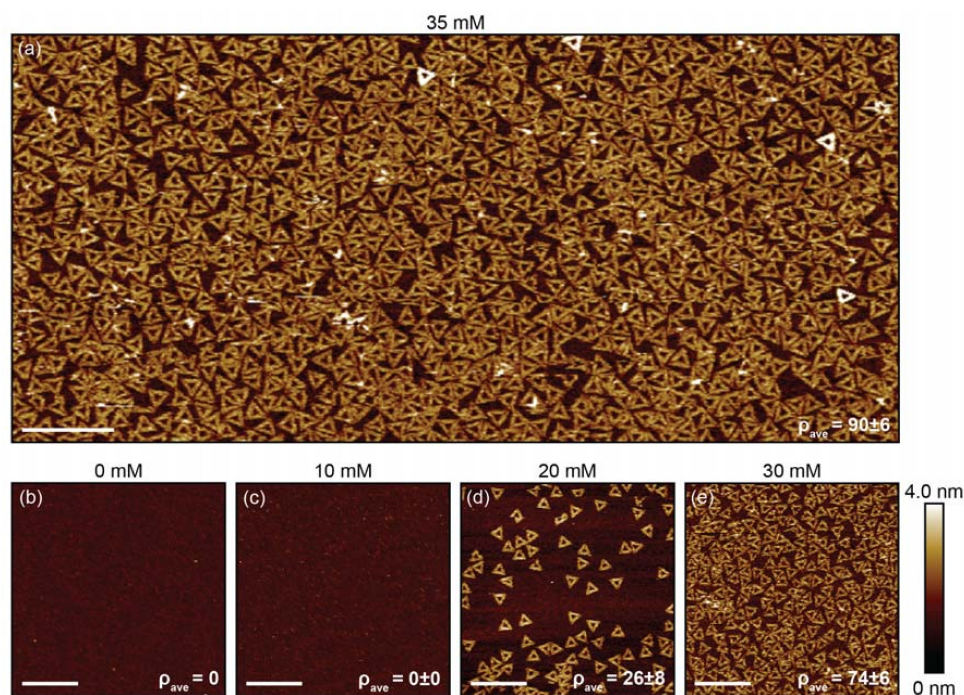


**Figure 2.** Atomic force microscopy (AFM) images of DNA origami triangles adsorbed onto boron-implanted silicon substrates. Prior to the DNA origami triangle deposition, the samples were cleaned with Piranha + hydrofluoric acid (HF). For all conditions, the deposition buffers were 10 mM bis-tris hydrochloric acid (HCl) with a pH of 6.6 and the deposition incubation time was  $\sim 24$  h. The  $\text{MgCl}_2$  concentration ( $[\text{MgCl}_2]$ ) for (a) was 35 mM. The average surface density increased from 0 to  $90 \pm 6/\mu\text{m}^2$  as the  $[\text{MgCl}_2]$  increased from 0 to 35 mM. Scale bars are 500 nm.

Physical adsorption of DNA origami was studied for a fixed  $[\text{MgCl}_2]$  of 35 mM in a deposition buffer pH range between 5.8 and 8.3 on the boron-implanted silicon substrate and a thermally grown  $\text{SiO}_2$  substrate (Figure 3). The average surface density range of 39 to 49 nanostructures per  $\mu\text{m}^2$  was observed on the boron-implanted silicon surface. In comparison, the surface density was significantly lower for the thermally grown  $\text{SiO}_2$  substrate, showing nearly zero adsorption at pH values between 5.8 and 7.2, and  $\sim 40$  nanostructures per  $\mu\text{m}^2$  at a pH value of 8.3. For consistency, the thermally grown  $\text{SiO}_2$  substrate was also cleaned with Piranha + HF, which was not expected to completely remove the 100 nm thick oxide. The surface density seen in Figure 3b is lower compared to Figure 2a due to different incubation periods of  $\sim 1$  h and  $\sim 24$  h, respectively. For an expanded DNA origami adsorption dataset, see the atomic force microscopy (AFM) images in Supplement S8. The relationship between the DNA origami adsorption and the thickness of the boron-rich amorphous oxide on the boron-implanted silicon substrates is shown in Supplement S9. These data indicate that selective adsorption of DNA origami should be possible on a substrate with lithographically defined boron-implanted silicon features that are separated by a  $\text{SiO}_2$  matrix.

To test this hypothesis and demonstrate selective adsorption, DNA origami triangles were then deposited onto a patterned substrate with boron-implanted silicon features, including  $1 \mu\text{m} \times 1 \mu\text{m}$  and  $5 \mu\text{m} \times 5 \mu\text{m}$  in size wells, separated by a 100 nm thick, thermally grown  $\text{SiO}_2$  matrix. An optical image of the patterned wafer is shown in Supplement S2. The substrates were cleaned with Piranha + HF, and then DNA origami was deposited from a deposition buffer with an optimized pH of 6.6 and  $[\text{MgCl}_2]$  of 35 mM. As shown in Figure 4, selective adsorption of DNA origami was achieved

on boron-implanted silicon features but not on the SiO<sub>2</sub> matrix. Unlike Gopinath et al. [30], spatial homogeneity was observed in the corners, edges, and interior of the patterned features, reflecting bulk adsorption from the solution, rather than 2D surface diffusion-limited coverage.

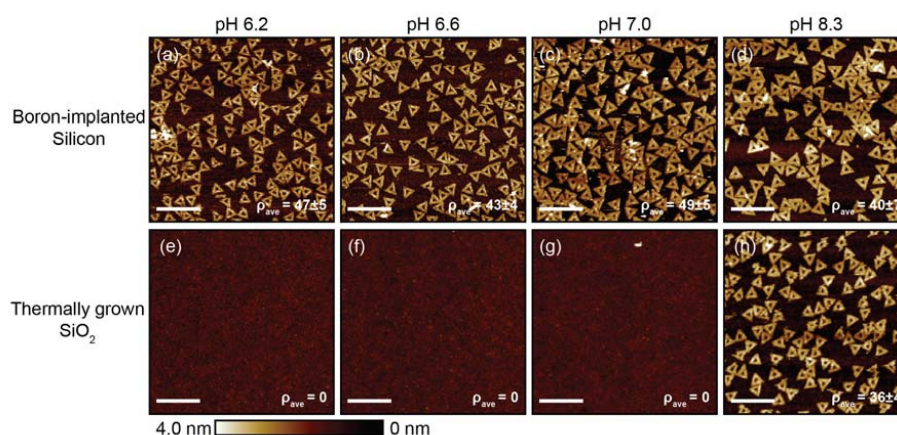


**Figure 3.** AFM images of DNA origami triangles adsorbed onto boron-implanted silicon substrates (a–d) and thermally grown silicon dioxide (SiO<sub>2</sub>) substrates (e–h) as a function of deposition buffer pH. The substrates were cleaned with Piranha + HF. For the pH values below 8.3, the deposition buffer was 10 mM bis-tris HCl with a [MgCl<sub>2</sub>] of 35 mM. For the pH value of 8.3, 1× tris-acetate-ethylenediaminetetraacetic acid (EDTA) with a [MgCl<sub>2</sub>] of 35 mM was selected to stay within the buffer range. For all conditions, the deposition incubation time was ~1 h. Scale bars are 500 nm.

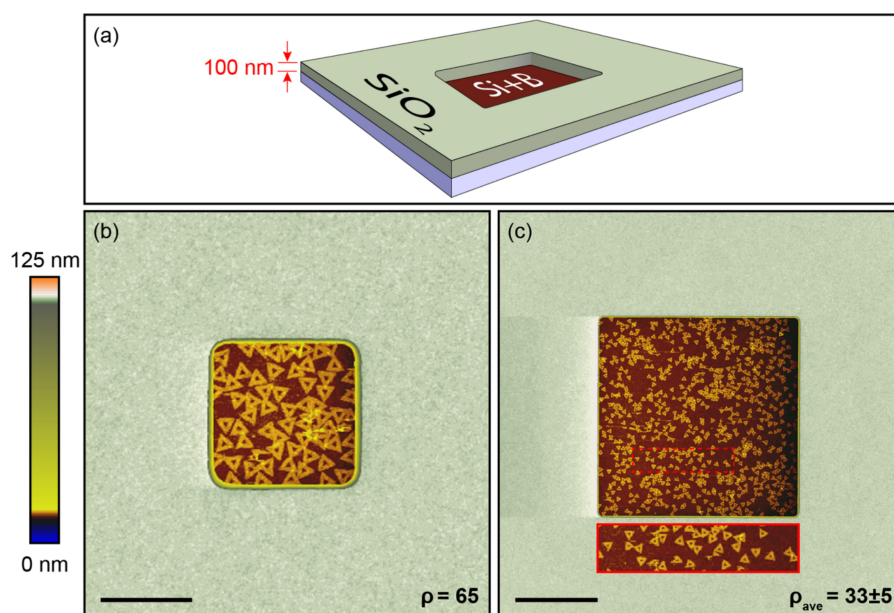


**Figure 4.** Schematic of a boron-implanted silicon feature surrounded by 100 nm thick SiO<sub>2</sub> (a). AFM height images of lithographically fabricated 1 μm × 1 μm (b) and 5 μm × 5 μm (c) boron-implanted silicon features surrounded with SiO<sub>2</sub>. The z-axis color scale was adjusted to show nanometer-scale contrast both within the well and on SiO<sub>2</sub> (100 nm above the well). The deposition buffer was 10 mM bis-tris HCl, with a pH of 6.6, and a [MgCl<sub>2</sub>] of 35 mM. DNA origami triangles adsorbed with a surface density of 65/μm<sup>2</sup> in (b) and 33 ± 5/μm<sup>2</sup> in (c) on the boron-implanted silicon surfaces, while no DNA origami adsorbed onto the SiO<sub>2</sub> surfaces. The rectangular insert is a 2× magnified image of the boron-implanted silicon surface shown in (c). For both samples, the deposition incubation time was ~1 h. Scale bars are 600 nm for (b) and 2 μm for (c).

### 3. Discussion

Physical adsorption of charged nanostructures in an electrolyte on silicon substrates is extremely complicated and includes pH-dependent specific ion effects on the structure and density of water and ions at the surface [43,44]. However, all pH values studied here are above the isoelectric point for SiO<sub>2</sub>, and the results are consistent with behavior described by Derjaguin, Landau, Verwey, and Overbeek (DLVO) theory [45,46], where deposition, or the lack thereof, is due to a net electrostatic attraction or repulsion between the substrate and the DNA origami nanostructures. Briefly, in the DNA origami buffer solution, an electric double layer forms around both the DNA origami, and at the boron-silicon surface. The thicknesses of both double layers depend on the electrostatic screening of ions in solution, particularly divalent Mg, and can include complex contributions from multiple forces [46]. In simple terms, this electric double layer creates repulsive electrostatic interactions between the origami and surface. Increased electrostatic screening from increasing cation concentrations allows the repulsive barrier to be overcome, and structures become bound through van der Waals interactions. However, at our Mg concentrations, the DNA origami themselves exhibit minimal aggregation; but for Mg concentrations over ~20 mM at pH 6.6, the electrostatic repulsion between the DNA origami and the boron-implanted silicon surface is sufficiently reduced to allow adsorption. In contrast, the electric double layer of the thermal oxide, and thus, its repulsive electric potential barrier, is strongly dependent on the pH-dependent surface concentration of silanol-groups and adsorption of hydrated Mg ions [44]. Based on the work of Ong et al. [47], we calculated that ~20% of the silanol-groups at the surface would be deprotonated between pH values of 5.8 to 7.2. In comparison, at a pH value of 8.3, ~50% of the silanol-groups were deprotonated, giving rise to a more negative surface charge (see Supplement S10 for the derivation), increasing adsorption of hydrated Mg ions, and reducing the barrier for DNA origami adsorption. This is consistent with the pH-dependent deposition results, which are summarized in Figure 5.

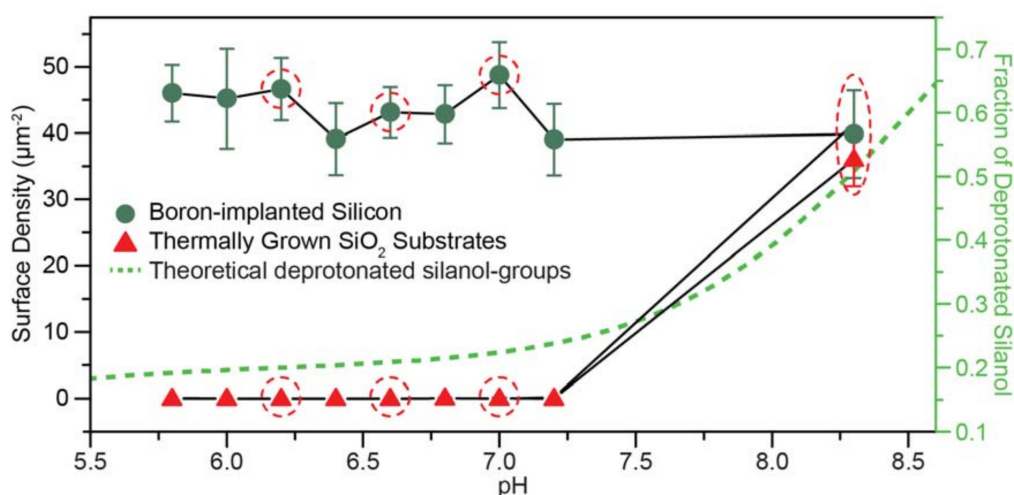


**Figure 5.** DNA origami surface density on boron-implanted silicon substrates oxide (green circle) and thermally grown SiO<sub>2</sub> substrates (red triangle) as a function of deposition buffer pH. Representative data points for the AFM images in Figure 3 are highlighted with red circles, and the theoretical population fraction of deprotonated silanol-groups on the oxide surfaces is depicted with a green dotted line.

### 4. Materials and Methods

#### 4.1. DNA Origami Synthesis

The DNA origami triangle design was adopted/adapted from a previously reported study [24]. The design was modified to include 6 fluorescent 5' FAM dyes (Integrated DNA

Technologies, Skokie, IL, USA) to facilitate sample purification. DNA origami triangles were self-assembled from single-stranded scaffolds (Bayou Biolabs, Metairie, LA, USA), sourced from the M13mp18 bacteriophage, and staple strands (Integrated DNA Technologies, Skokie, IL, USA). The DNA scaffolds and corresponding staples were mixed in a 1:10 molar ratio, in a 1× tris-acetate-ethylenediaminetetraacetic acid (EDTA) buffer (Fisher Scientific, Hampton, NH, USA), with a pH of 8.3, and a [MgCl<sub>2</sub>] of 12.5 mM. The mixture was annealed at 70 °C for 20 min and then cooled to 20 °C at a rate of 0.6 °C/min. Well-formed nanostructures were purified using rate-zonal centrifugation as described in Supplement S1 [48,49]. After purification, the solution was normalized to a 5 nM concentration and stored in 5 µL aliquots at −80 °C to minimize sample degradation.

#### 4.2. Substrate Cleaning

Silicon substrates were sonicated in deionized water, followed by 100% acetone (KMG, Fort Worth, TX, USA), and then 100% isopropanol (KMG, Fort Worth, TX, USA). The substrates were then sequentially soaked in Piranha to remove the organic contaminants and then 1:100 HF (Fisher Scientific, Hampton, NH, USA), to remove the surface oxide. For additional details, see Supplement S1.

#### 4.3. DNA Origami Deposition

First, 20 µL of a deposition buffer was added to a 5 µL DNA origami solution with a 5 nM concentration. Once combined, the solution was gently pipette mixed. Cleaned silicon substrates were individually placed inside a petri dish (Fisher Scientific, Hampton, NH, USA) on top of a general-purpose lab wipe that was soaked in a deposition buffer so as to combat evaporation and subsequent change in the concentration of the deposited DNA solution. Then 25 µL of the DNA origami mixture was deposited onto the silicon substrates within 40 min of their cleaning, but before the native oxide grew back (Supplement S11). After deposition, the petri dish was sealed to minimize evaporation during incubation and sample transport between labs. For the MgCl<sub>2</sub> concentration screening experiments, boron-implanted silicon samples were incubated at room temperature for ~24 h. For the pH screening experiments and the DNA origami deposition onto patterned substrates with boron-implanted silicon features, samples were incubated at room temperature for ~1 h. The DNA origami surface density on Piranha + HF cleaned boron-implanted silicon substrates, as a function of incubation time, is shown in Supplement S6. After incubation, excess DNA origami was removed by gravity-assisted rinsing, see Supplement S1.

#### 4.4. Determining Surface Density

With the exception of boron-implanted silicon features surrounded by a raised SiO<sub>2</sub> matrix, three high-resolution 5 µm × 5 µm images were captured in fluid AFM (Dimension FastScan, Bruker, Santa Barbara, CA, USA). Each image was divided into twenty-five 1 µm × 1 µm squares, and the number of DNA origami triangles in each square was manually counted. The average number of DNA nanostructures per 1 µm × 1 µm square is indicated by the average surface density.

### 5. Conclusions

Physical adsorption of DNA nanostructures was demonstrated on boron-implanted silicon substrates. While the average surface density was statistically comparable to natural mica, the adsorption uniformity was greater. The surface density dramatically increased from 0–91 nanostructures per µm<sup>2</sup> as the salt concentration of the deposition buffer increased from 0–35 mM. Adsorption was also pH independent on the boron-implanted silicon surfaces, for the range we tested. The adsorption contrast between the boron-implanted silicon surface and SiO<sub>2</sub> was optimized in a deposition buffer pH range of 5.8–7.2 at a [MgCl<sub>2</sub>] of 35 mM. In support of prior experiments, deprotonated silanol-groups at elevated pH in the presence of hydrated Mg ions promoted extensive binding between DNA origami and the oxide surfaces. Surface electrostatics provided by boron implantation enabled DNA adsorption, but further research is necessary to fully understand the

electrochemical interactions controlling DNA origami deposition. Recommended next steps include further characterization of the boron-silicon surface structure, exploring how adsorption varies as a function of the feature size, and tuning the binding strength through mono and divalent cation concentrations to enable formation of ordered DNA origami arrays within the boron-implanted silicon wells [50–52].

**Supplementary Materials:** Supplementary materials can be found at <http://www.mdpi.com/1422-0067/19/9/2513/s1>.

**Author Contributions:** Conceptualization—S.S., W.L.H.; Methodology—S.T., J.F.-E.; Formal Analysis—S.T., S.K., J.F.-E., E.S.; Investigation—S.T., S.K., J.F.-E., E.S.; Resources—S.S.; Data Curation—S.T., S.K., J.F.-E., E.S.; Writing—Original Draft Preparation—S.T.; Writing—Review & Editing—S.T., S.K., J.E.P., L.C.G., E.G., W.K., S.S., W.L.H.; Visualization—S.T., E.G., W.L.H.; Supervision—S.S., E.G., W.L.H.; Project Administration—W.L.H.; Funding Acquisition—E.G., W.K., S.S., W.L.H.

**Funding:** This research was funded in part by the National Science Foundation (CMMI 1344915 and ECCS 1807809), the Semiconductor Research Corporation, and the National Institutes of Health (NIH K25GM093233 from the National Institute of General Medical Sciences).

**Acknowledgments:** (A) the Process Development team at Micron Technology for fabricating the patterned substrate; (B) Shu Qin at Micron Technology for developing the boron implant process; (C) Daniel Kelly for helping clean the wafers at Boise State; (D) William Bill Knowlton and Mike Hurley at Boise State for useful discussions; (E) Ashwin Gopinath and Paul Wilhelm Karl Rothemund at Caltech for technical insight, (F) Yaqiao Wu and the Center for Advanced Energy Studies-Microscopy and Characterization Suite (CAES-MaCS) in Idaho Falls for the FIB sample preparation and TEM imaging, and (G) the Surface Science Laboratory at Boise State for AFM sample characterization.

**Conflicts of Interest:** The authors declare no conflicts of interest.

## Abbreviations

DNA	deoxyribonucleic acid
SiO <sub>2</sub>	silicon dioxide
MgCl <sub>2</sub>	magnesium chloride
[MgCl <sub>2</sub> ]	magnesium chloride concentration
SADP	self-aligned double patterning
SAQP	self-aligned quadruple patterning
DSA	directed self-assembly
BCP	block copolymers
DSA-BCP	block copolymer directed self-assembly
APTES	aminopropyltrimethoxysilane
HMDS	hexamethyldisilazane
SAM	self-assembled monolayer
XPS	X-ray Photoelectron Spectroscopy
SIMS	Secondary Ion Mass Spectroscopy
TEM	Transmission Electron Microscopy
FIB	focused-ion beam
HF	hydrofluoric acid
FFT	Fast Fourier Transform
HCl	hydrochloric acid
AFM	atomic force microscopy
EDTA	ethylenediaminetetraacetic acid
FAM	fluorescein amidite

## References

1. Moore, G.E. Cramping more components onto integrated circuits. *Electronics* **1965**, *38*, 114–117. [[CrossRef](#)]
2. Moore, G.E. Progress in digital integrated electronics. *Int. Electron Devices Meet.* **1975**, *21*, 11–13; reprinted in *IEEE Solid-State Circuits Soc. Newsl.* **2006**, *11*, 36–37. [[CrossRef](#)]

3. Gallatin, G. Nanofabrication: A perspective from litho practitioners. In Proceedings of the SRC/IBM/ONR Workshop on Bio-Nanofabrication and Materials, San Jose, CA, USA, 16–17 November 2016.
4. Xu, K.; Souriau, L.; Hellin, D.; Versluijs, J.; Wong, P.; Vangoidsenhoven, D.; Vandenbroeck, N.; Dekkers, H.; Shi, X.; Albert, J.; et al. Key contributors for improvement of line width roughness, line edge roughness, and critical dimension uniformity: 15 nm half-pitch patterning with extreme ultraviolet and self-aligned double patterning. *J. Micro Nanolithogr. MEMS MOEMS* **2013**, *12*, 041302. [[CrossRef](#)]
5. Kodama, C.; Ichikawa, H.; Nakayama, K.; Nakajima, F.; Nojima, S.; Kotani, T.; Ihara, T.; Takahashi, A. Self-Aligned Double and Quadruple Patterning Aware Grid Routing Methods. *IEEE Trans. Comput. Des. Integr. Circuits Syst.* **2015**, *34*, 753–765. [[CrossRef](#)]
6. Wu, B.; Kumar, A. *Extreme Ultraviolet Lithography*; McGraw-Hill: New York, NY, USA, 2009; pp. 12–34, ISBN 9780071549189.
7. Mimotogi, S. Extension of patterning technologies down to sub-10nm half pitch. *Proc. SPIE* **2013**, *8685*, 868503–868509.
8. SemiSynBio Consortium and Roadmap Development. Available online: <https://www.src.org/program/grc/semisynbio/semisynbio-consortium-roadmap/> (accessed on 28 July 2017).
9. International Technology Roadmap for Semiconductors 2.0 2015 Edition. Available online: <http://www.itrs2.net/itrs-reports.html> (accessed on 20 October 2017).
10. Quader, K.N. Flash Memory at a Cross-Road: Challenges and Opportunities. In Proceedings of the 2012 4th IEEE International Memory Workshop, Milan, Italy, 20 March 2012; IEEE: Piscataway, NJ, USA, 2012; pp. 1–4.
11. Edwards, E.W.; Müller, M.; Stoykovich, M.P.; Solak, H.H.; de Pablo, J.J.; Nealey, P.F. Dimensions and Shapes of Block Copolymer Domains Assembled on Lithographically Defined Chemically Patterned Substrates. *Macromolecules* **2007**, *40*, 90–96. [[CrossRef](#)]
12. Seeman, N.C. DNA in a material world. *Nature* **2003**, *421*, 427–431. [[CrossRef](#)] [[PubMed](#)]
13. Deng, Z.; Mao, C. Molecular Lithography with DNA Nanostructures. *Angew. Chem. Int. Ed.* **2004**, *43*, 4068–4070. [[CrossRef](#)] [[PubMed](#)]
14. He, Y.; Ye, T.; Ribbe, A.E.; Mao, C. DNA-Templated Fabrication of Two-Dimensional Metallic Nanostructures by Thermal Evaporation Coating. *J. Am. Chem. Soc.* **2011**, *133*, 1742–1744. [[CrossRef](#)] [[PubMed](#)]
15. Ma, X.; Huh, J.; Park, W.; Lee, L.P.; Kwon, Y.J.; Sim, S.J. Gold nanocrystals with DNA-directed morphologies. *Nat. Commun.* **2016**, *7*, 12873. [[CrossRef](#)] [[PubMed](#)]
16. Bates, F.S.; Fredrickson, G.H. Block Copolymer Thermodynamics: Theory and Experiment. *Annu. Rev. Phys. Chem.* **1990**, *41*, 525–557. [[CrossRef](#)] [[PubMed](#)]
17. Digne, C.T.; Brun, C.; Gasparutto, D.; Baillin, X.; Tiron, R. DNA Origami Mask for Sub-Ten-Nanometer Lithography. *ACS Nano* **2016**, *10*, 6458–6463. [[CrossRef](#)] [[PubMed](#)]
18. Surwade, S.P.; Zhou, F.; Wei, B.; Sun, W.; Powell, A.; O'Donnell, C.; Yin, P.; Liu, H. Nanoscale Growth and Patterning of Inorganic Oxides Using DNA Nanostructure Templates. *J. Am. Chem. Soc.* **2013**, *135*, 6778–6781. [[CrossRef](#)] [[PubMed](#)]
19. Shen, B.; Linko, V.; Tapio, K.; Kostianen, M.A.; Toppari, J.J. Custom-shaped metal nanostructures based on DNA origami silhouettes. *Nanoscale* **2015**, *7*, 11267–11272. [[CrossRef](#)] [[PubMed](#)]
20. Zhou, F.; Sun, W.; Ricardo, K.B.; Wang, D.; Shen, J.; Yin, P.; Liu, H. Programmably Shaped Carbon Nanostructure from Shape-Conserving Carbonization of DNA. *ACS Nano* **2016**, *10*, 3069–3077. [[CrossRef](#)] [[PubMed](#)]
21. Ke, Y.; Ong, L.L.; Shih, W.M.; Yin, P. Three-Dimensional Structures Self-Assembled from DNA Bricks. *Science* **2012**, *338*, 1177–1183. [[CrossRef](#)] [[PubMed](#)]
22. Mandelkern, M.; Elias, J.G.; Eden, D.; Crothers, D.M. The dimensions of DNA in solution. *J. Mol. Biol.* **1981**, *152*, 153–161. [[CrossRef](#)]
23. Green, C.M.; Schutt, K.; Morris, N.; Zadegan, R.M.; Hughes, W.L.; Kuang, W.; Graugnard, E. Metrology of DNA arrays by super-resolution microscopy. *Nanoscale* **2017**, *9*, 10205–10211. [[CrossRef](#)] [[PubMed](#)]
24. Rothmund, P.W.K. Folding DNA to create nanoscale shapes and patterns. *Nature* **2006**, *440*, 297–302. [[CrossRef](#)] [[PubMed](#)]
25. Scheible, M.B.; Ong, L.L.; Woehrstein, J.B.; Jungmann, R.; Yin, P.; Simmel, F.C. A Compact DNA Cube with Side Length 10 nm. *Small* **2015**, *11*, 5200–5205. [[CrossRef](#)] [[PubMed](#)]

26. Jin, Z.; Sun, W.; Ke, Y.; Shih, C.-J.; Paulus, G.L.C.; Hua Wang, Q.; Mu, B.; Yin, P.; Strano, M.S. Metallized DNA nanolithography for encoding and transferring spatial information for graphene patterning. *Nat. Commun.* **2013**, *4*, 1663. [[CrossRef](#)] [[PubMed](#)]
27. Surwade, S.P.; Zhao, S.; Liu, H. Molecular Lithography through DNA-Mediated Etching and Masking of SiO<sub>2</sub>. *J. Am. Chem. Soc.* **2011**, *133*, 11868–11871. [[CrossRef](#)] [[PubMed](#)]
28. Zhou, F.; Michael, B.; Surwade, S.P.; Ricardo, K.B.; Zhao, S.; Liu, H. Mechanistic Study of the Nanoscale Negative-Tone Pattern Transfer from DNA Nanostructures to SiO<sub>2</sub>. *Chem. Mater.* **2015**, *27*, 1692–1698. [[CrossRef](#)]
29. Sarveswaran, K.; Gao, B.; Kim, K.N.; Bernstein, G.H.; Lieberman, M. Adhesion of DNA nanostructures and DNA origami to lithographically patterned self-assembled monolayers on Si[100]. In *Alternative Lithographic Technologies II*; Herr, D.J.C., Ed.; International Society for Optics and Photonics: Bellingham, WA, USA, 2010; p. 76370M.
30. Gopinath, A.; Rothmund, P.W.K. Optimized Assembly and Covalent Coupling of Single-Molecule DNA Origami Nanoarrays. *ACS Nano* **2014**, *8*, 12030–12040. [[CrossRef](#)] [[PubMed](#)]
31. Love, J.C.; Estroff, L.A.; Kriebel, J.K.; Nuzzo, R.G.; Whitesides, G.M. Self-Assembled Monolayers of Thiolates on Metals as a Form of Nanotechnology. *Chem. Rev.* **2005**, *105*, 1103–1170. [[CrossRef](#)] [[PubMed](#)]
32. Kershner, R.J.; Bozano, L.D.; Micheel, C.M.; Hung, A.M.; Fornof, A.R.; Cha, J.N.; Rettner, C.T.; Bersani, M.; Frommer, J.; Rothmund, P.W.K.; et al. Placement and orientation of individual DNA shapes on lithographically patterned surfaces. *Nat. Nanotechnol.* **2009**, *4*, 557–561. [[CrossRef](#)] [[PubMed](#)]
33. Tanaka, S.; Taniguchi, M.; Kawai, T. Selective Adsorption of DNA onto SiO<sub>2</sub> Surface in SiO<sub>2</sub>/SiH Pattern. *Jpn. J. Appl. Phys.* **2004**, *43*, 7346–7349. [[CrossRef](#)]
34. Amodio, A.; Adedeji, A.F.; Castronovo, M.; Franco, E.; Ricci, F. pH-Controlled Assembly of DNA Tiles. *J. Am. Chem. Soc.* **2016**, *138*, 12735–12738. [[CrossRef](#)] [[PubMed](#)]
35. Billingsley, D.J.; Lee, A.J.; Johansson, N.A.B.; Walton, A.; Stanger, L.; Crampton, N.; Bonass, W.A.; Thomson, N.H. Patchiness of ion-exchanged mica revealed by DNA binding dynamics at short length scales. *Nanotechnology* **2014**, *25*, 025704. [[CrossRef](#)] [[PubMed](#)]
36. Whittle, K.M.; Vick, G.L. Control of Boron Diffusion from a Pyrolytic Borosilicate Glass Source. *J. Electrochem. Soc.* **1969**, *116*, 645–648. [[CrossRef](#)]
37. Sadigh, B.; Lenosky, T.J.; Caturla, M.-J.; Quong, A.A.; Benedict, L.X.; Diaz de la Rubia, T.; Giles, M.M.; Foad, M.; Spataru, C.D.; Louie, S.G. Large enhancement of boron solubility in silicon due to biaxial stress. *Appl. Phys. Lett.* **2002**, *80*, 4738–4740. [[CrossRef](#)]
38. Vick, G.L.; Whittle, K.M. Solid Solubility and Diffusion Coefficients of Boron in Silicon. *J. Electrochem. Soc.* **1969**, *116*, 1142–1144. [[CrossRef](#)]
39. Brown, D.M.; Kennicott, P.R. Glass Source Diffusion in Si and SiO<sub>2</sub>. *J. Electrochem. Soc.* **1971**, *118*, 293–300. [[CrossRef](#)]
40. Busen, K.M.; FitzGibbons, W.A.; Tsang, W.K. Ellipsometric Investigations of Boron-Rich Layers on Silicon. *J. Electrochem. Soc.* **1968**, *115*, 291–294. [[CrossRef](#)]
41. Tenney, A.S.; Ghezzi, M. Etch Rates of Doped Oxides in Solutions of Buffered HF. *J. Electrochem. Soc.* **1973**, *120*, 1091–1095. [[CrossRef](#)]
42. Fujii, M.; Sugimoto, H.; Hasegawa, M.; Imakita, K. Silicon nanocrystals with high boron and phosphorus concentration hydrophilic shell—Raman scattering and X-ray photoelectron spectroscopic studies. *J. Appl. Phys.* **2014**, *115*, 084301. [[CrossRef](#)]
43. Zhang, X.G. *Electrochemistry of Silicon and Its Oxide*; Kluwer Academic/Plenum Publishers: New York, NY, USA, 2001; pp. 45–89, ISBN 0-306-46541-8.
44. DeWalt-Kerian, E.L.; Kim, S.; Azam, M.S.; Zeng, H.; Liu, Q.; Gibbs, J.M. pH-Dependent Inversion of Hofmeister Trends in the Water Structure of the Electrical Double Layer. *J. Phys. Chem. Lett.* **2017**, *8*, 2855–2861. [[CrossRef](#)] [[PubMed](#)]
45. Besra, L.; Liu, M. A review on fundamentals and applications of electrophoretic deposition (EPD). *Prog. Mater. Sci.* **2007**, *52*, 1–61. [[CrossRef](#)]
46. Boström, M.; Deniz, V.; Franks, G.V.; Ninham, B.W. Extended DLVO theory: Electrostatic and non-electrostatic forces in oxide suspensions. *Adv. Colloid Interface Sci.* **2006**, *123*, 5–15. [[CrossRef](#)] [[PubMed](#)]
47. Ong, S.; Zhao, X.; Eisenthal, K.B. Polarization of water molecules at a charged interface: Second harmonic studies of the silica/water interface. *Chem. Phys. Lett.* **1992**, *191*, 327–335. [[CrossRef](#)]

48. Zhirnov, V.; Zadegan, R.M.; Sandhu, G.S.; Church, G.M.; Hughes, W.L. Nucleic acid memory. *Nat. Mater.* **2016**, *15*, 366–370. [[CrossRef](#)] [[PubMed](#)]
49. Lin, C.; Perrault, S.D.; Kwak, M.; Graf, F.; Shih, W.M. Purification of DNA-origami nanostructures by rate-zonal centrifugation. *Nucleic Acids Res.* **2013**, *41*, e40. [[CrossRef](#)] [[PubMed](#)]
50. Aghebat Rafat, A.; Pirzer, T.; Scheible, M.B.; Kostina, A.; Simmel, F.C. Surface-assisted large-scale ordering of DNA origami tiles. *Angew. Chem. Int. Ed. Engl.* **2014**, *53*, 7665–7668. [[CrossRef](#)] [[PubMed](#)]
51. Kocabey, S.; Kempter, S.; List, J.; Xing, Y.; Bae, W.; Schiffels, D.; Shih, W.M.; Simmel, F.C.; Liedl, T. Membrane-Assisted Growth of DNA Origami Nanostructure Arrays. *ACS Nano* **2015**, *9*, 3530–3539. [[CrossRef](#)] [[PubMed](#)]
52. Woo, S.; Rothmund, P.W.K. Self-assembly of two-dimensional DNA origami lattices using cation-controlled surface diffusion. *Nat. Commun.* **2014**, *5*, 4889. [[CrossRef](#)] [[PubMed](#)]



© 2018 by the authors. Licensee MDPI, Basel, Switzerland. This article is an open access article distributed under the terms and conditions of the Creative Commons Attribution (CC BY) license (<http://creativecommons.org/licenses/by/4.0/>).